pp. 1–10 (2012)

Modelling of bioimpedance measurements: unstructured mesh application to real human anatomy

A. A. DANILOV*, D. V. NIKOLAEV†, S. G. RUDNEV*,
V. Yu. SALAMATOVA‡, and Yu. V. VASSILEVSKI*

Abstract — A technology for high-resolution efficient numerical modelling of bioimpedance measurements is considered that includes 3D image segmentation, adaptive unstructured tetrahedral mesh generation, finite-element discretization, and analysis of simulation data. The first-order convergence of the proposed numerical methods on a series of unmatched meshes and roughly second-order convergence on a series of nested meshes are shown. The current, potential, and sensitivity field distributions are computed for conventional schemes of bioimpedance measurements using segmented geometrical torso model of the Visible Human Project (VHP) man. Use of the adaptive tetrahedral meshes reduces significantly the number of mesh elements and, hence, the associated computational cost compared to rectangular meshes while keeping the model accuracy.

Measurements of the electrical impedance of a biological tissue in response to an applied alternating current provide a number of non-invasive, harmless, portable, and relatively low-cost techniques for use in medical and biological studies [4,9,12]. An example is the application of bioelectric impedance analysis (BIA) for *in vivo* human body composition assessment [17,19]. In BIA, a simple representation of the human body as a homogeneous isotropic cylindrical conductor is commonly used. The electrical impedance Z is converted to the volume of conducting space V, i.e., a volume of water containing electrolytes that conduct the electrical current in the body, using the formula

$$V = \rho \frac{L^2}{Z}$$

where ρ is the resistivity, and L the conductor length. The ratio L^2/Z is called the impedance index. Thomasset [24] and Hoffer [10] were the first to show a high correlation of the impedance index with the total body water volume and, thus, opened the way for using bioimpedance in body composition studies. Its numerous applications include the assessment of the body fluid balance, nutritional status, associated health risks, and prognosis [13, 18, 22, 32].

---

*Institute of Numerical Mathematics, Russian Academy of Sciences, Moscow 119333, Russia. Email: a.a.danilov@gmail.com

†Scientific Research Center ‘Medass’, Moscow 101000, Russia

‡Scientific-Educational Center of the Institute of Numerical Mathematics, Russian Academy of Sciences, Moscow 119333, Russia

This work has been supported in part by RFBR (grants no. 11-01-00971, 10-01-91055), and the Federal Program ‘Academic and pedagogical staff of innovative Russia’.

The same methodological principle is applied in impedance cardiography (ICG) for the assessment of central hemodynamics and also in impedance plethysmography (IPG) for the evaluation of peripheral vascular function [4]. In contrast to electrical impedance tomography aimed at visualization of the internal body structure (see, e.g., [3, 12]), a little amount of electrodes is used in BIA, ICG, and IPG with a wide spectrum of electrode types, their properties and configurations (local, whole-body, segmental, polysegmental) and measurement frequencies. This inspires an idea of optimization of bioimpedance measurements for specific purposes. Since a real human body represents a complex non-homogeneous and non-isotropic medium with a variable cross-section area, the fundamental issues are the nature and relative contribution of various organs and tissues to the bioimpedance signal. The latter, as well as the measurement optimization problem, were studied by means of impedance simulations using computerized models of the real human anatomy (see, e.g., [1, 15, 30]). A similar approach is also used in radiography, nuclear medicine, radiation protection, and other research areas [2, 29].

Modelling sensitivity distributions for various measurement schemes requires solving a number of computational problems using high-resolution anatomically accurate 3D models. Our aim was to describe unstructured mesh generation and computational modelling procedures for bioimpedance measurements, to characterize the convergence of the suggested numerical method, and to illustrate the current, potential, and sensitivity field distributions for a conventional bioimpedance measurement scheme using a high-resolution geometrical model of the human body. The paper represents an extension of our previously published work [25].

The outline of the paper is as following. In Section 2 we consider a mathematical model. In Section 3 we analyse the convergence of the proposed numerical methods on simplified meshes. In Section 4 we describe the mesh generation process for the real human anatomy. In Section 5 we provide some numerical results.

1. Mathematical model

As described in [9], the electrical fields generated during bioimpedance measurements are governed by the equation

$$\operatorname{div}(\mathbf{C}\nabla U) = 0 \quad \text{in } \Omega \tag{1.1}$$

with the boundary conditions

$$(\mathbf{J},\mathbf{n}) = \pm I_0/S_\pm \quad \text{on } \Gamma_\pm \tag{1.2}$$

$$(\mathbf{J},\mathbf{n}) = 0 \quad \text{on } \partial\Omega\backslash\Gamma_\pm \tag{1.3}$$

$$U(x_0,y_0,z_0) = 0 \tag{1.4}$$

$$\mathbf{J} = \mathbf{C}\nabla U \tag{1.5}$$

where Ω is the computational domain, $\partial\Omega$ is its boundary, $\Gamma_\pm$ are the electrode contact surfaces, $\mathbf{n}$ is an external unit normal vector, U is the electric potential, $\mathbf{C}$

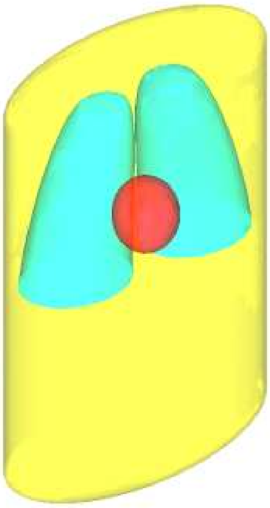

Figure 1. Simplified geometrical model of a human torso.

is the conductivity tensor, $\mathbf{J}$ is the current density, I_0 is the electric current, $S_\pm$ are the areas of the electrode contacts. Equation (1.1) determines the distribution of the electric field in the domain with heterogeneous conductivity $\mathbf{C}$. Equation (1.2) sets a constant current density on the electrode contact surfaces. Equation (1.3) defines the no-flow condition on the boundary. The uniqueness of the solution is guaranteed by equation (1.4), where (x_0, y_0, z_0) is some point in the domain Ω.

Discretization of (1.1)–(1.5) was obtained using a finite element scheme with piecewise linear elements P1 on unstructured tetrahedral meshes [33].

2. Convergence study

We consider a simple geometrical model of a human torso which was described previously in [25] (see Fig. 1) and a series of unstructured tetrahedral meshes with a variable element size. Having the automatic mesh generation algorithm for this model, we can perform a lot of numerical tests. For each mesh we compute the numerical solution and compare it with the numerical solution obtained on the finest mesh by using L_2-norm to evaluate the difference between the numerical solutions. Since different meshes may consist of different vertex sets, we apply a conventional piecewise-linear interpolation from a coarse mesh to a fine mesh, and compute the discrete L_2-norm on the fine mesh. It should be noted that an extra interpolation error is added in the case of two unmatched meshes as compared to hierarchical meshes. We consider both series of unmatched unstructured meshes and of hierarchical meshes.

The numerical results of the convergence study with unmatched meshes are presented in Fig. 2. The numerical solution obtained on the finest mesh with the maximal element size 5 mm is considered as a control solution. Solutions on other

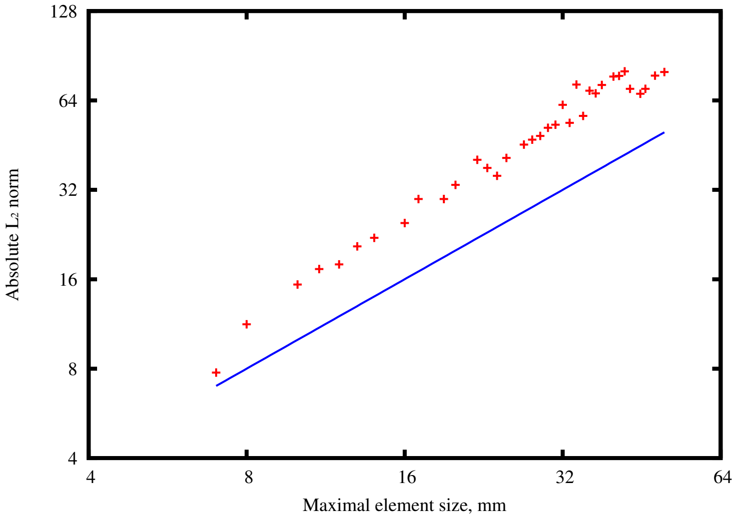

Figure 2. Convergence study on the series of unmatched meshes.

Table 1.
The results of convergence study on hierarchical meshes.

N_V	N_T	Memory, MB	N_{it}	Time, s	L_2-norm
2032	9359	7.16	13	0.02	1.24E-03
14221	74872	37.3	23	0.18	9.31E-04
106509	598976	299.1	58	3.70	5.07E-04
824777	4791808	2437.5	127	68.55	1.53E-04
6492497	38334464	20015.3	353	2634.15	–

meshes with maximal element size from 7 mm to 50 mm are compared to this control solution. The values in Fig. 2 are well distributed along the line parallel to the bisector of the coordinate axes of the absolute L_2 norm and the maximal element size h, meaning that the proposed method demonstrates the first-order convergence on unmatched meshes.

Now we consider the series of hierarchical meshes. The initial coarse mesh contains 9359 tetrahedrons. Starting from this mesh, we split each tetrahedron into 8 smaller tetrahedra by splitting each face into four triangles by the middle points on the edges [33]. We call this operation a uniform refinement of the mesh. Now we can apply uniform refinement to the new mesh, and so on. At each step the element size of the mesh decreases by half. The vertex set of the finest mesh fully covers the vertex sets of all previous meshes, meaning that the extra interpolation errors are not introduced in L_2-norm computation. The finest mesh in the series of five meshes has more than 38 million tetrahedrons and requires nearly 20 GB of memory for computation. We used a GMRES-based iterative linear solver with the second-order ILU preconditioner [14, 33].

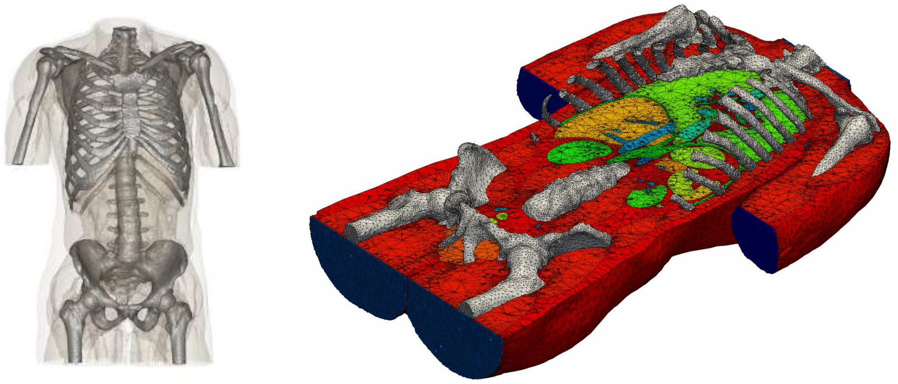

Figure 3. Geometrical model of the segmented image (left) and unstructured tetrahedral mesh (right).

The results of the convergence study on the series of hierarchical meshes are presented in Table 1. The first two columns show the number of vertices N_V and the number of tetrahedrons N_T. The next three columns show the memory usage, the number of linear solver iterations N_{it} needed for 10^{12}-fold reduction of an initial residual, and the overall time use, respectively. The last column contains the relative L_2-norm that reduces asymptotically with roughly the second-order convergence.

In summary, our tests demonstrated the first-order convergence of the proposed numerical methods on a series of unmatched meshes and nearly the second-order convergence on a series of nested meshes.

3. Mesh generation

The original 3D image of the human torso was derived from the VHP-man data [27]. The data represent an array of 567×305×843 colored voxels with the resolution 1×1×1 mm. The initial segmented model of the VHP human torso was kindly provided by the Voxel-Man group [11]. This model has been produced primarily for visualization purposes, it contained a significant amount of unclassified tissue and, thus, was not entirely suited for numerical purposes. Therefore, a further processing of the segmented model was needed. It was performed semi-automatically using the ITK-SNAP segmentation software program [31]. At the final stage, we used several post-processing algorithms for filling the remaining gaps between the tissues and final segmented data smoothing.

The resulting geometrical model of the torso was used to create an unstructured tetrahedral mesh. This can be achieved using several approaches, including the marching cubes algorithm for surface reconstruction [28], surface triangulation smoothing and coarsening [23, 26], 3D Delaunay triangulation [6], and the advancing front technique for volume mesh generation [5, 6]. We applied the Delaunay triangulation algorithm from the CGAL-Mesh library [21]. This algorithm makes it possible to define a specific mesh size for each model material. In order to preserve the geometrical features of the segmented model, while keeping a feasible number

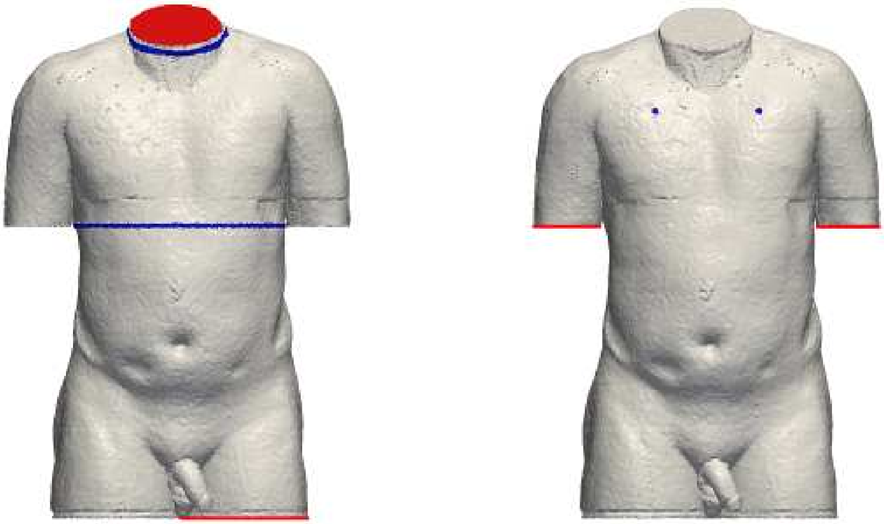

Figure 4. Electrode configurations for Kubicek-like (left) and Mozhaev (right) measurement schemes: current electrodes in red, voltage electrodes in blue.

of vertices, we have assigned a smaller mesh size to blood vessels and a larger mesh size to fat and muscle tissues.

The segmented model, which contains 26 labels and describes the major organs and tissues of the human torso, and the generated mesh with 413 508 vertices and 2 315 329 tetrahedrons are depicted in Fig. 3. This mesh retains most anatomical features of the human torso.

After mesh generation, we added a skin layer and multilayer electrodes to the surface of the constructed mesh. Boundary triangulation was used to create a prismatic mesh on the surface, and then each prism was split into three tetrahedrons resulting in a conformal mesh. Mesh cosmetics algorithms from the Ani3D library [33] were used to improve the mesh quality. This essential step reduces discretization errors and the condition number of the resulting systems of linear equations.

4. Numerical results

Let us consider two electrode configuration schemes: the Kubicek-like scheme (see [16]) with a pair of current electrodes on the head and the left leg, and a pair of band voltage electrodes as illustrated in Fig. 4 (left), and a scheme by Mozhaev [20] with a pair of current electrodes on the arms and a pair of spot voltage electrodes on the chest as shown in Fig. 4 (right). Since our calculations were performed on a torso segmented model, we applied the boundary conditions (1.2) at the appropriate interfaces.

We defined the conductivity parameters for labeled tissues using the data in [7]. The simulations were done for current frequencies 5 and 50 kHz. The computed

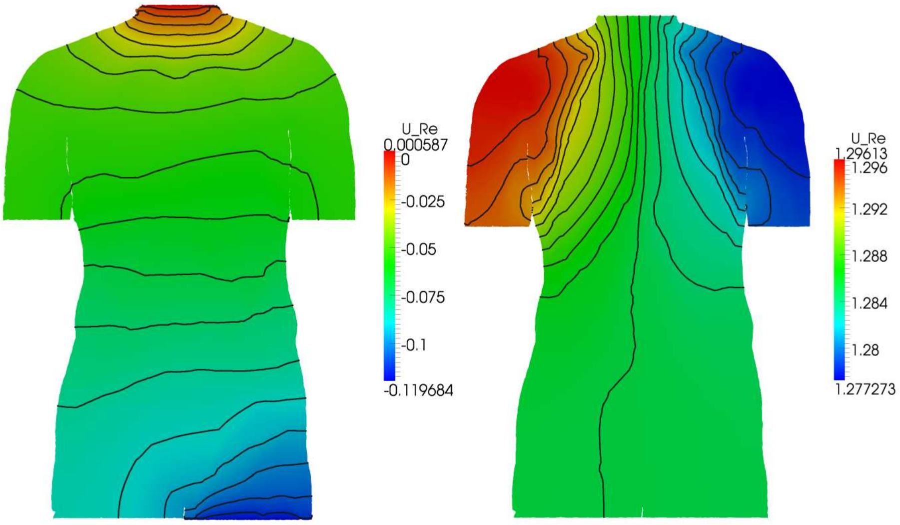

Figure 5. Cutplanes of the potential fields. Measurement frequency 50 kHz.

Figure 6. Current lines. Measurement frequency 5 kHz.

current and potential field distributions are shown in Figs. 5 and 6. The results of sensitivity analysis showing the contribution of various body regions and tissues to the measured impedance signal (for methodology, see [8]) are presented in Fig. 7 and Table 2 and show good quantitative agreement with the results obtained by Kauppinen et al. [15] and Mozhaev [20].

Figure 7. Areas of high sensitivity providing 70% of the whole sensitivities. Measurement frequency 50 kHz.

Table 2.
Relative contribution (%) of organs and tissues to the impedance signal.

	Kubicek-like scheme		Mozhaev scheme	
	5 kHz	50 kHz	5 kHz	50 kHz
Muscles	72.56	69.44	53.14	45.93
Left lung	5.23	5.49	9.81	10.39
Right lung	4.59	5.03	12.62	13.44
Diaphragm	2.57	2.39	2.81	2.58
Oesophagus	2.27	2.00	2.23	2.18
Stomach	2.19	2.14	1.29	1.23
Thyroid gland	1.61	1.50	0.86	0.80
Visceral fat	1.25	0.54	1.67	1.51
Intestine	0.91	1.12	1.58	1.76
Trachea	0.68	0.71	0.55	0.53
Heart	0.64	1.01	3.50	5.02
Bones	0.57	0.51	1.50	1.34
Pancreas	0.47	0.45	0.38	0.36
Liver	0.28	0.50	0.41	0.69
Skin	0.23	0.22	0.00	0.26
Pulmonary trunk	0.05	0.11	0.43	0.67
Pulmonary veins	0.15	0.28	0.92	1.66
Pulmonary arteries	0.15	0.28	0.88	1.58
Other arteries	0.75	1.50	1.55	2.31
Other veins	2.21	4.18	2.82	4.77
Other tissues	0.64	0.60	1.05	0.99

5. Conclusion

In this work, the unstructured tetrahedral mesh generation technology for real human anatomy, as well as the method of numerical modelling of bioimpedance measurements on such meshes, are considered. The numerical results on a simplified human torso model demonstrate at least first-order convergence of the proposed scheme. Sensitivity distribution analysis for a pair of conventional measurement schemes on the segmented torso VHP geometrical model showed good quantitative agreement with the results obtained previously by other authors. The suggested approach enables mesh generation for high-resolution models with a significantly fewer mesh elements compared to rectangular meshes. This reduces the computational cost of solving various problems, such as the development of new bioimpedance measurement schemes, optimization of electrode placement configurations, their types, and measurement frequencies.

References

1. L. Beckmann, D. van Riesen, and S. Leonhardt, Optimal electrode placement and frequency range selection for the detection of lung water using bioimpedance spectroscopy In: *Proc. 29th Annual Int. Conf. of the IEEE, Aug. 22–26*, 2007, pp. 2685–2688.
2. M. Caon, Voxel-based computational models of real human anatomy: a review. *Radiat. Environ. Biophys.* (2004) **42**, No. 4, 229–235.
3. V. Cherepenin, A. Karpov, A. Korjenevsky et al., Three-dimensional EIT imaging of breast tissues: system design and clinical testing. *IEEE Trans. Med. Imaging* (2002) **21**, No. 6, 662–667.
4. G. Cybulski, *Ambulatory Impedance Cardiography*. Springer-Verlag, Berlin, Heidelberg, 2011.
5. A. A. Danilov, Unstructured tetrahedral mesh generation technology. *Comp. Math. Math. Phys.* (2010) **50**, No. 1, 139–156.
6. P. J. Frey and P. L. George, *Mesh Generation: Application to Finite Elements*. Hermes Science, Paris, Oxford, 2000.
7. C. Gabriel, A. Peyman, and E. Grant, Electrical conductivity of tissues at frequencies below 1 MHz. *Phys. Med. Biol.* (2009) **54**, No. 16, 4863–4878.
8. D. B. Geselowitz, An application of electrocardiographic lead theory to impedance plethysmography. *IEEE Trans. Biomed. Eng.* (1971) **18**, No. 1, 38–41.
9. S. Grimnes and O. G. Martinsen, *Bioimpedance and Bioelectricity Basics*. Elsevier, Amsterdam, 2008.
10. E. C. Hoffer, C. K. Meador, and D. C. Simpson, Correlation of whole-body impedance with total body water volume. *J. Appl. Physiol.* (1969) **27**, No. 4, 531–534.
11. K. H. Höhne, B. Pflesser, A. Pommert et al., A realistic model of human structure from the Visible Human data. *Meth. Inform. Med.* (2001) **40**, No. 2, 83–89.
12. D. S. Holder, *Electrical Impedance Tomography*. Bristol, Philadelphia, Institute of Physics Publishers, 2005.
13. I. Janssen, S. B. Heymsfield, and R. Ross, Low relative skeletal muscle mass (sarcopenia) in older persons is associated with functional impairment and physical disability. *J. Am. Ger. Soc.* (2002) **50**, No. 5, 889–896.
14. I. E. Kaporin, High quality preconditioning of a general symmetric positive definite matrix based on its $U^tU+U^tR+R^tU$-decomposition. *Numer. Linear Algebra Appl.* (1998) **5**, No. 6, 483–509.
15. P. K. Kauppinen, J. A. Hyttinen, and J. A. Malmivuo, Sensitivity distributions of impedance cardiography using band and spot electrodes analyzed by a three-dimensional computer model. *Ann. Biomed. Engrg.* (1998) **26**, No. 4, 694–702.

16. W. G. Kubicek, Impedance plethysmograph. *Pat. USA 3.340.867. A61b.502*, 1967, Sept. 12.
17. R. F. Kushner and D. A. Schoeller, Estimation of total body water by bioelectrical impedance analysis. *Am. J. Clin. Nutr.* (1986) **44**, No. 3, 417–424.
18. U. G. Kyle, I. Bosaeus, A. De Lorenzo et al., Bioelectrical impedance analysis, part II: Utilization in clinical practice. *Clin. Nutr.* (2004) **23**, No. 6, 1430–1453.
19. H. C. Lukaski, P. E. Johnson, W. W. Bolonchuk, and G. I. Lykken, Assessment of fat-free mass using bioelectrical impedance measurements of the human body. *Am. J. Clin. Nutr.* (1985) **41**, No. 4, 810–817.
20. V. A. Mozhaev, Sensitivity analysis of polysegmental BIA parameters for estimation of body composition and systemic hydrohemodynamics. In: *IFMBE Proceedings* (2007) **17**, No. 3, 44–47.
21. L. Rineau and M. Yvinec, A generic software design for Delaunay refinement meshing. *Comp. Geom. Theory Appl.* (2007) **38**, No. 1-2, 100–110.
22. P. B. Soeters, P. L. M. Reijven, M. A. E. van Bokhorst-de van der Schueren et al., A rational approach to nutritional assessment. *Clin. Nutr.* (2008) **27**, No. 5, 706–716.
23. G. Taubin, A signal processing approach to fair surface design. In: *Proc. of the 22nd Annual Conf. on Comp. Graphics and Interactive Techniques*, 1995, ACM, New York, 351–358.
24. A. Thomasset, Bioelectric properties of tissue impedance measurement in clinical medicine. Significance of curves obtained. *Lyon Med.* (1962) **94**, 107–118 (in French).
25. Yu. V. Vassilevski, A. A. Danilov, D. V. Nikolaev et al., Finite-element analysis of bioimpedance measurements. *Zh. Vych. Mat. Matem. Fiz.* (2012) **52**, No. 4, 733–745 (in Russian).
26. Yu. V. Vassilevski, A. V. Vershinin, A. A. Danilov, and A. V. Plenkin, *Tetrahedral Mesh Generation in Domains Defined in CAD Systems*. Inst. Num. Math., Moscow, 2005, 21–32 (in Russian).
27. *The Visible Human Project*, http://www.nlm.nih.gov/research/visible/visible_human.html
28. Z. Wu and J. M. Sullivan, Multiple material marching cubes algorithm. *Int. J. Numer. Meth. Eng.* (2003) **58**, No. 2, 189–207.
29. X. G. Xu and K. F. Eckerman, *Handbook of Anatomical Models for Radiation Dosimetry*. CRC Press, Boca Raton, 2009.
30. F. Yang and R. P. Patterson, A simulation study on the effect of thoracic conductivity inhomogeneities on sensitivity distributions. *Ann. Biomed. Eng.* (2008) **36**, No. 5, 762–768.
31. P. A. Yushkevich, J. Piven, H. C. Hazlett et al. User-guided 3D active contour segmentation of anatomical structures: Significantly improved efficiency and reliability. *Neuroimage* (2006) **31**, No. 3, 1116–1128.
32. S. Zhu, Z. Wang, W. Shen, S. B. Heymsfield, and S. Heshka, Percentage body fat ranges associated with metabolic syndrome risk: results based on the Third National Health and Nutrition Examination Survey (1988–1994). *Am. J. Clin. Nutr.* (2003) **78**, No. 2, 228–235.
33. *3D Generator of Anisotropic Meshes*, http://sourceforge.net/projects/ani3d